Journal of Solid State Chemistry 184 (2011) 1445–1450

Contents lists available at ScienceDirect

Journal of Solid State Chemistry

journal homepage: www.elsevier.com/locate/jssc

$[R\text{-}C_7H_{16}N_2][V_2Te_2O_{10}]$ and $[S\text{-}C_7H_{16}N_2][V_2Te_2O_{10}]$; new polar templated vanadium tellurite enantiomers

Ethan C. Glor [a], Samuel M. Blau [a], Jeongho Yeon [c], Matthias Zeller [b], P. Shiv Halasyamani [c], Joshua Schrier [a], Alexander J. Norquist [a,*]

[a] *Department of Chemistry, Haverford College, PA 19041, USA*
[b] *Department of Chemistry, Youngstown State University, Youngstown, OH 44555, USA*
[c] *Department of Chemistry, University of Houston, Houston, TX 77204, USA*

ARTICLE INFO

Article history:
Received 3 November 2010
Received in revised form
28 February 2011
Accepted 7 April 2011
Available online 14 April 2011

Keywords:
Vanadium
Tellurite
Stereoactive lone pairs
Iterative Hirshfeld
Dipole moment

ABSTRACT

New polar vanadium tellurite enantiomers have been synthesized under mild hydrothermal conditions through the use of sodium metavanadate, sodium tellurite and enantiomerically pure sources of either *R*-3-aminioquinuclidine or *S*-3-aminioquinuclidine. $[R\text{-}C_7H_{16}N_2][V_2Te_2O_{10}]$ and $[S\text{-}C_7H_{16}N_2][V_2Te_2O_{10}]$ contain $[V_2Te_2O_{10}]_n^{2n-}$ layers constructed from $[(VO_2)_2O(TeO_4)_2]$ monomers. Steric effects associated with the hydrogen-bonding network between the $[V_2Te_2O_{10}]_n^{2n-}$ layers and $[C_7H_{16}N_2]^{2+}$ result in polar structures and crystallization in the space group $P2_1$ (no. 4). Electron localization functions were calculated to visualize the tellurite stereoactive lone pairs. Both iterative and non-iterative Hirshfeld techniques were evaluated as means to determine atomic partial charges, with iterative Hirshfeld charges more accurately representing charge distributions in the reported enantiomers. These charges were used to calculate both component and *net* dipole moments. $[R\text{-}C_7H_{16}N_2][V_2Te_2O_{10}]$ and $[S\text{-}C_7H_{16}N_2][V_2Te_2O_{10}]$ exhibit dipole moments of 17.37 and 16.62*D*, respectively. $[R\text{-}C_7H_{16}N_2][V_2Te_2O_{10}]$ and $[S\text{-}C_7H_{16}N_2][V_2Te_2O_{10}]$ both display type 1 phase-matching capabilities and exhibit second harmonic generation activities of $\sim 50 \times \alpha\text{-}SiO_2$.

1. Introduction

Materials that possess crystallographic noncentrosymmetry are of great interest to researchers because they can exhibit several desirable physical properties [1], such as second harmonic generation (SHG) and piezoelectricity. Specific attention is paid to compounds that crystallize in one of the ten polar crystal classes, which results in a permanent dipole moment and enables the possibility of ferroelectricity [2] and pyroelectricity [3].

The strategies that are most commonly employed for the creation of new polar materials involve the use of asymmetric building units [4–10]. Specific approaches include the use of d^0 early transition metals (Ti^{4+}, V^{5+}, Mo^{6+}, etc.) and lone pair cations (such as Sn^{2+}, Sb^{3+}, Se^{4+}, etc.), which adopt asymmetric geometries in oxide coordination environments owing to second-order Jahn–Teller distortions [11–13]. Vanadium selenites and tellurites have been the focus of recent attention, owing to the presence of multiple asymmetric building units [7,14–21]. In addition, the metal oxide bonds contained in such compounds exhibit high polarizabilities, and are the suspected sources of the unusually high SHG responses in materials such as $KTiOPO_4$ (KTP) [22,23] and $LiNbO_3$ [24]. Other example systems include the use of early transition metal oxide fluoride anions [25–27], the synthesis of organic frameworks containing asymmetric linkers [28,29] and the preparation of new borates [30–32].

Two fundamental questions are posed by the formation of a new polar material. First, why is the compound polar? Identification of the interactions that induce polarity is paramount in understanding the formation mechanisms of the given material. Second, how do the component dipole moments contribute to the *net* moment in the compound? This information requires one to calculate both component and *net* dipole moments and to analyze the mechanisms of their partial (or total) cancellation. While the symmetry of a given material generally dictates the orientation of the *net* dipole moment, the magnitudes and directions of component dipole moments in polar structures are of great interest because the degree of their cancellation significantly impacts many properties, such as second harmonic generation [33,34].

The strategy employed in this study utilizes three low symmetry building units: a chiral organic amine, V^{5+} and Te^{4+}. We report on the synthesis, structure and characterization of a pair of new polar enantiomers, $[R\text{-}C_7H_{16}N_2][V_2Te_2O_{10}]$ and $[S\text{-}C_7H_{16}N_2][V_2Te_2O_{10}]$.

---

* Corresponding author. Fax: +1 610 896 4963.
E-mail address: anorquis@haverford.edu (A.J. Norquist).

0022-4596/$ - see front matter © 2011 Elsevier Inc. All rights reserved.
doi:10.1016/j.jssc.2011.04.016

Electron localization functions [35,36], and both component and net dipole moments are calculated for each enantiomer, and their respective SHG activities are reported.

2. Experimental

2.1. Materials

$NaVO_3$ (99.5%), Na_2TeO_3 (99.5%), (*R*)-(+)-3-aminoquinuclidine dihydrochloride (98%, *R*-aqn) and (*S*)-(-)-3-aminoquinuclidine dihydrochloride (98%, *S*-aqn) were purchased from Aldrich and used as received. Deionized water was used in these syntheses.

2.2. Synthesis

All reactions were conducted in 15 mL polypropylene screw top bottles. The pH of each reaction gel was adjusted to 8 using 2 M HCl and it was stirred for 10 min before heating at 90 °C for 60 h. Bottles were opened in air, and products were recovered through filtration. Powder X-ray diffraction patterns of each bulk sample match the pattern generated from the respective single-crystal X-ray structure data.

$[R\text{-}C_7H_{16}N_2][V_2Te_2O_{10}]$ (**1a**) was synthesized through the reaction of 0.1532 g (1.26×10^{-3} mol) of $NaVO_3$, 0.2789 (1.32×10^{-3} mol) of Na_2TeO_3, 0.1639 g (1.30×10^{-3} mol) of *R*-aqn and 6.05 g (3.36×10^{-1} mol) of deionized water. Yellow rods were obtained in 61% yield, based on Te. Elemental microanalysis for **1a** obsd (calc): C 13.36(13.02); H 2.46(2.50); N 4.29(4.30); V 15.12(15.79); Te 38.31(39.56). IR data: N–H 1470, 1525, 1634 cm^{-1}, C–H 3008 cm^{-1}, V=O 863 cm^{-1}, Te–O–Te 657 cm^{-1}.

$[S\text{-}C_7H_{16}N_2][V_2Te_2O_{10}]$ (**1b**) was synthesized through the reaction of 0.1537 g (1.26×10^{-3} mol) of $NaVO_3$, 0.1668 (7.88×10^{-4} mol) of Na_2TeO_3, 0.1670 g (1.33×10^{-3} mol) of *S*-aqn and 5.99 g (3.33×10^{-1} mol) of deionized water. Yellow rods were obtained in 47% yield, based on Te. Elemental microanalysis for **1b** obsd (calc): C 13.32(13.02); H 2.40(2.50); N 4.29(4.30); V 15.02(15.79); Te 37.24(39.56). IR data: N–H 1470, 1525, 1635 cm^{-1}, C–H 3008 cm^{-1}, V=O 863 cm^{-1}, Te–O–Te 658 cm^{-1}.

2.3. Single crystal X-ray diffraction

Data were collected using a Bruker AXS Smart Apex CCD diffractometer with Mo*K*α radiation (λ=0.71073 Å). Single crystals were mounted on a Mitegen micromesh mount using a trace of mineral oil and cooled *in-situ* to 100(2) K for data collection. Frames were collected, indexed, processed and the files scaled and corrected for absorption using APEX2 [37]. The heavy atom positions were determined using SIR92 [38]. All other non-hydrogen sites were located from Fourier difference maps. All non-hydrogen sites were refined using anisotropic thermal parameters using full matrix least squares procedures on F_o^2 with $I>3\sigma(I)$. Hydrogen atoms were placed in geometrically idealized positions. All calculations were performed using Crystals [39]. Relevant crystallographic data are listed in Table 1.

2.4. Powder X-ray diffraction

Powder diffraction patterns were recorded on a GBC-Difftech MMA powder diffractometer. Samples were mounted on aluminum plates. Calculated powder patterns were generated from single crystal data using ATOMS *v.* 6.0 [40].

2.5. Infrared spectroscopy

Infrared measurements were obtained using a Perkin Elmer FT-IR Spectrum 1000 spectrophotometer. Samples were diluted with spectroscopic grade KBr and pressed into a pellet. Scans were run over the range of 400–4000 cm^{-1}.

Table 1
Crystallographic data for **1a** and **1b.**

Compound	$[R\text{-}C_7H_{16}N_2][V_2Te_2O_{10}]$ (1a)	$[S\text{-}C_7H_{16}N_2][V_2Te_2O_{10}]$ (1b)
Formula	$C_7H_{16}N_2O_{10}Te_2V_2$	$C_7H_{16}N_2O_{10}Te_2V_2$
fw	645.29	645.29
Space-group	$P2_1$ (No. 4)	$P2_1$ (No. 4)
a (Å)	6.0376(10)	6.0405(11)
b (Å)	20.075(3)	20.084(4)
c (Å)	6.1332(10)	6.1369(11)
β (°)	97.071(2)	97.094(3)
V ($Å^3$)	737.7(2)	738.8(2)
Z	2	2
ρ_{calc} ($g\ cm^{-3}$)	2.905	2.901
λ (Å)	0.71073	0.71073
T (K)	100(2)	100(2)
μ (mm^{-1})	5.198	5.191
Flack parameter	0.02(3)	−0.02(4)
R_1[a]	0.0274	0.0373
WR_2[b]	0.0621	0.0765

[a] $R_1=\Sigma||F_o|-F_c||/\Sigma|F_o|$.
[b] $WR_2=[\Sigma W(F_o^2-F_c^2)^2/[\Sigma W(F_o^2)^2]^{1/2}$.

2.6. Thermogravimetric analysis

Thermogravimetric analyses (TGA) were conducted using a Q500 thermogravimetric analyzer from TA instruments. Samples were contained within a platinum crucible and heated in nitrogen at 10 °C min^{-1} to 950 °C. TGA traces are available in the Supplementary Data.

2.7. Nonlinear optical measurements

Powder SHG measurements were conducted using a modified Kurtz-NLO system, with a 1064 nm light source [33,41]. Polycrystalline $[R\text{-}C_7H_{16}N_2][V_2Te_2O_{10}]$ (**1a**) and $[S\text{-}C_7H_{16}N_2][V_2Te_2O_{10}]$ (**1b**) were ground and sieved into distinct particle size ranges: <20, 20–45, 45–63, 63–75, 75–90 and 90–120 μm. Crystalline α-SiO_2 was ground and sieved into identical particle size ranges in order to compare the SHG properties of **1a** and **1b** to known materials. All powders were placed in separate capillary tubes, and no index-matching fluid was used in any experiment. The SHG, i.e. 532 nm light, was collected in reflection and detected using a photomultiplier tube. A 532 nm narrow-bandpass interference filter was attached to the tube in order to only detect the SHG light.

3. Calculations

3.1. Electron localization functions (ELFs)

Solid-state electronic structure calculations were performed using version 47 of the Stuttgart tight-binding linear muffin-tin orbital, atomic sphere approximation (TB-LMTO-ASA) code [35,36], which replaces the core electrons with a pseudopotential. It is known that the valence-electron-density ELF quantitatively differs from all-electron values, but does not alter the qualitative results except for the lack of core basins [42]. To focus more clearly on the anion, only the $[V_2Te_2O_{10}]$ components (using the experimental crystal structure) were included in these calculations. We have previously demonstrated that amines do not modify the location of the Te lone pair [43]. Consequently, the discussion of ELF isosurfaces will be restricted to qualitative properties.

3.2. Partial charges and dipole moments

Solid-state electronic structure calculations were performed using ABINIT 6.0.3 [44,45], using the Perdew–Burke–Ernzerhof generalized gradient approximation (PBE-GGA) exchange-correlation functional, norm-conserving Trollier–Martins pseudopotentials, a planewave basis set with an energy cutoff of 25 hartrees and utilizing the experimental crystal structures. Calculations using Te pseudopotentials both with and without 4*d*-electrons included in the valence were performed. Small differences in atomic charges were observed, on the order of 9%. All charges and dipole moments presented below were calculated from Te pseudopotentials that included Te 4*d* electrons. Sampling of the Brillouin zone was performed with a $6\times6\times6$ Monkhorst-Pack grid. Hirshfeld [46] and iterative Hirshfeld (Hirshfeld-I) [47,48] atomic partial charge determinations were performed on the self-consistent valence electron density using the Cut3D program and promolecule all-electron atomic charge densities generated using the HF96 atomic Hartree–Fock code [49]. Dipole moments were calculated from the partial charges and atomic positions using a methodology described earlier [9,25,26].

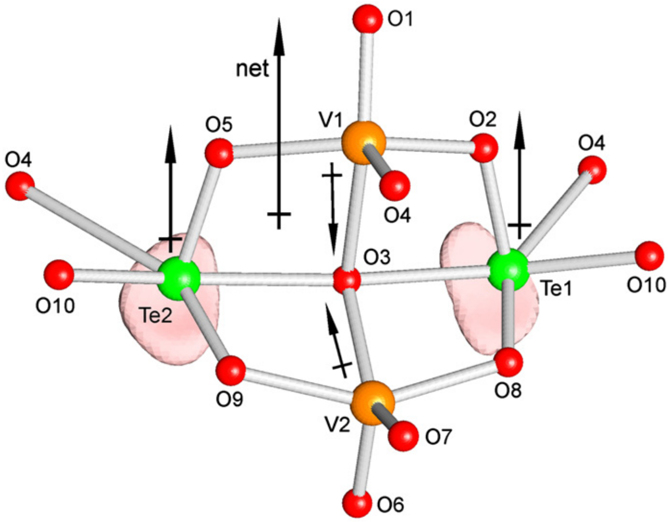

Fig. 1. Ball-and-stick representation of the $[(VO_2)_2O(TeO_4)_2]$ monomers in **1a** and **1b**. ELF isosurfaces are shown with a boundary condition of 0.78. The black arrows indicate the approximate directions and magnitudes of the dipole moments for the TeO_5 and VO_5 polyhedra. The large black arrow represents the direction of the net dipole of the $[(VO_2)_2O(TeO_4)_2]$ monomer.

4. Results and discussion

$[R\text{-}C_7H_{16}N_2][V_2Te_2O_{10}]$ (**1a**) and $[S\text{-}C_7H_{16}N_2][V_2Te_2O_{10}]$ (**1b**) are enantiomers. As such, their respective connectivities are identical, with each being the inverse of the other. Their inorganic components are constructed from $[(VO_2)_2O(TeO_4)_2]$ monomers that contain two $[VO_5]$ trigonal bipyramids and two $[TeO_5]$ distorted square pyramids, as shown in Fig. 1. These monomers are connected to one another through shared oxide ions, creating $[V_2Te_2O_{10}]_n^{2n-}$ layers. See Fig. 2.

While other reported templated vanadium tellurites [43,50–52] and hybrid compounds [53] contain either $[V_2Te_2O_{10}]_n^{2n-}$ chains or layers, those observed in **1a** and **1b** are novel. The chains present in $[C_4H_{14}N_2][V_2Te_2O_{10}]$ [43] and layers in $[C_2H_{10}N_2][VTeO_5]_2$ [50], $[C_2H_{10}N_2][(VO_2)(TeO_3)]\cdot H_2O$ [51], $[C_4H_{12}N_2][(VO_2)(TeO_3)]_2\cdot H_2O$ [51] and $(C_4H_{13}N_3)[(VO_2)(TeO_3)]_2\cdot 2H_2O$ [52] all contain tellurite dimers that are linked by $[VO_4]$ or $[VO_5]$ polyhedra, with no observed V–O–V connections. The layers present in $Cu(C_{14}H_8N_4)V_2Te_2O_{10}$ [53] and $Cu(C_{18}H_{10}N_4)V_2Te_2O_{10}$ [53] contain Cu–O–Te linkages and distinctly different layer topologies.

The $V–O_{terminal}$ bonds in **1a** and **1b** are short, ranging between 1.628(6) and 1.667(7) Å, while $V–O_{bridging}$ bonds vary more widely and are generally longer with an observed range of 1.907(5)–2.174(9) Å. The *intra*-monomer Te–O bonds range between 1.884(5) and 2.337(5) Å. Longer Te–O–V connections are observed between monomers, with long Te–O bonds (2.694(4)–2.782(4) Å) and short V–O bonds (1.642(6)–1.651(6) Å). Selected bond lengths are given in Table 2 and 3.

1a and **1b** were analyzed using bond valence sums [54,55]. The calculated ΣS_i values for each cation correspond to their assigned oxidation states, with V^{5+} and Te^{4+} sums ranging between 4.94 and 5.00 and between 4.10 and 4.14, respectively. The second-order Jahn–Teller (SOJT) [11–13] distortions in the Te^{4+} cations are manifested in their asymmetric coordination geometries. Full tables of calculated bond valence sums are given in Supplementary Data.

Table 2
Selected bond lengths (Å) in $[R\text{-}C_7H_{16}N_2][V_2Te_2O_{10}]$ (**1a**).

V1–O1	1.632(4)	Te1–O2	1.887(4)
V1–O2	1.922(4)	Te1–O3	2.335(3)
V1–O3	2.150(6)	Te1–O4	2.694(4)
V1–O4	1.642(4)	Te1–O8	1.899(4)
V1–O5	1.910(3)	Te1–O10	1.964(3)
V2–O3	2.022(5)	Te2–O3	2.255(3)
V2–O6	1.640(4)	Te2–O4	2.782(4)
V2–O7	1.656(4)	Te2–O5	1.886(3)
V2–O8	1.945(3)	Te2–O9	1.897(4)
V2–O9	1.947(3)	Te2–O10	1.964(3)

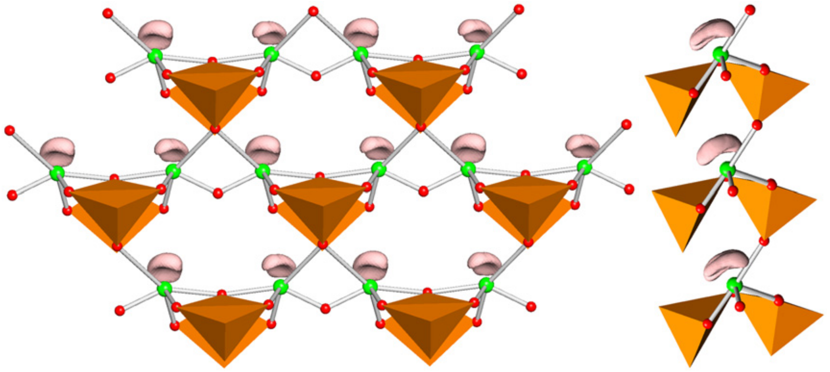

Fig. 2. The $[V_2Te_2O_{10}]_n^{2n-}$ layers in **1a** and **1b**. ELF isosurfaces are shown with a boundary condition of 0.78.

Table 3
Selected bond lengths (Å) in [S-$C_7H_{16}N_2$][$V_2Te_2O_{10}$] (**1b**).

V1–O1	1.628(6)	Te1–O2	1.886(5)
V1–O2	1.907(5)	Te1–O3	2.258(4)
V1–O3	2.174(9)	Te1–O4	2.781(6)
V1–O4	1.651(6)	Te1–O8	1.904(6)
V1–O5	1.926(6)	Te1–O10	1.968(5)
V2–O3	1.995(8)	Te2–O3	2.337(5)
V2–O6	1.639(6)	Te2–O4	2.698(6)
V2–O7	1.667(7)	Te2–O5	1.884(5)
V2–O8	1.955(6)	Te2–O9	1.907(6)
V2–O9	1.944(6)	Te2–O10	1.948(5)

Table 4
Calculated dipole moments in [R-$C_7H_{16}N_2$][$V_2Te_2O_{10}$] (**1a**) and [S-$C_7H_{16}N_2$][$V_2Te_2O_{10}$] (**1b**) using Hirshfeld-I charges.

[R-$C_7H_{16}N_2$][$V_2Te_2O_{10}$]		[S-$C_7H_{16}N_2$][$V_2Te_2O_{10}$]	
Species	Dipole moment (D)	Species	Dipole moment (D)
[V(1)O_5]	9.72	[V(1)O_5]	9.95
[V(2)O_5]	8.36	[V(2)O_5]	8.06
[Te(1)O_5]	13.56	[Te(2)O_5]	13.55
[Te(2)O_5]	12.49	[Te(1)O_5]	12.52
[$V_2Te_2O_{10}$]$_n^{2n-}$ layer	19.04	[$V_2Te_2O_{10}$]$_n^{2n-}$ layer	18.68
[R-aqnH_2]$^{2+}$	2.30	[S-aqnH_2]$^{2+}$	2.26
net moment	17.37	*net* moment	16.62

ELF isosurfaces were calculated for **1a** and **1b**. Lobelike, monosynaptic ELF basins are observed near each Te^{4+} cation, consistent with stereoactive lone pairs. Isosurfaces for the [$(VO_2)_2O(TeO_4)_2$] monomers and [$V_2Te_2O_{10}$]$_n^{2n-}$ layers in **1a** are shown in Fig. 1 and Fig. 2, respectively. While the ELFs are determined by the charge densities and their nodal characteristics, rather than electron pairing *per se* [56], they correspond to chemical intuitions of localized bonds and lone pairs [57]. All stereoactive lone pairs within a given [$V_2Te_2O_{10}$]$_n^{2n-}$ layer are roughly aligned for each structure (see Fig. 2).

There are many arbitrary methods of assigning atomic partial point charges. The Hirshfeld scheme has certain conceptual and technical advantages, but tends to underestimate the magnitude of the partial charges, a particularly relevant example being that of polyoxometallate anions recently studied by Courcot and Bridgeman [58]. This is corrected in the iterative Hirshfeld (Hirshfeld-I) scheme, described by Bultinck et al. [47,48] by self-consistently refining the promolecular atomic densities used in the partitioning calculation. Benchmarking studies on small molecules indicate that this corrects for the systematic defects of the (non-iterative) Hirshfeld scheme, and that the resulting charges yield accurate electrostatic potentials [59]. To our knowledge, the only prior application of the Hirshfeld-I scheme to periodic systems is the study of paramagnetic adsorbates on graphene by Leenaerts et al. [60]. The Hirshfeld-I scheme requires a set of neutral, cationic and anionic atomic charge densities; since atomic anions are unstable in GGA-PBE theory, Hartree–Fock theory was used to obtain the atomic promolecular charge densities. The partial charges calculated for both the iterative and the non-iterative schemes are shown in Tables S3 and S4 for **1a** and **1b**, respectively. As in the example of formaldehyde discussed by Bultinck et al. [47], the Hirshfeld-I partial charges are generally greater in magnitude than the non-iterative result. The vanadium charges calculated using the Hirshfeld-I scheme (1.603–1.688) are approximately fifteen times larger than the Hirshfeld charges (0.091–0.128). The tellurium charges increase by approximately three fold between the Hirshfeld-I (1.978–2.009) and Hirshfeld (0.607–0.613) schemes. Similar increases are observed in the oxygen charges for the Hirshfeld-I (-0.552 to -1.071) and Hirshfeld (-0.195 to -0.299) schemes. In each case, the Hirshfeld-I charges are in better agreement with chemical intuition. Increases are also observed in the nitrogen, carbon and hydrogen charges with one exception. C3 becomes slightly more positive from -0.0183 and -0.0167 in **1a** and **1b** to 0.006 and 0.002, respectively. The Hirshfeld-I partial charges appear to represent the charge distribution in these compounds more accurately.

Having obtained the atomic partial charges, dipole moments were calculated for each bond in **1a** and **1b**, using the Hirshfeld-I charges. Dipole moments were calculated for each [VO_5] and [TeO_5] polyhedron using Hirshfeld-I charges, and are shown in Fig. 1 as arrows. The direction and length of the arrows are representative of the calculated dipole moment vectors. The magnitudes of these vectors are listed in Table 4. As shown in Fig. 1, the dipole moments on the [VO_5] polyhedra are nearly aligned with the V–O3 bonds. The dipole moments on the two [VO_5] polyhedra in each [$(VO_2)_2O(TeO_4)_2$] monomer largely cancel with one another. In contrast, the dipole moments on the [TeO_5] polyhedra are more aligned. These moments point 'away' from the stereoactive lone pairs and toward the more negatively charged oxide ligands. The main components of the net dipole moments on the [$(VO_2)_2O(TeO_4)_2$] monomers are based upon the 'additive' [TeO_5] dipole moments. The calculated [TeO_5] dipole moments range between 12.27 and 13.56D, which is consistent with other reported values [9,61]. The small differences in partial atomic charges and both component and net dipole moments reflect small differences in atomic positions. As only the dipole moment components along the b-axis contribute to the net dipole moments of **1a** and **1b**, the small bond dipole magnitudes and orientation differences result in slightly different net dipole moments of the two enantiomers.

While it is known that chiral components are useful in the formation of new noncentrosymmetric materials [62–68], researchers often value compounds that crystallize in polar space groups more highly. Of the twenty-one noncentrosymmetric crystal classes, only the ten polar crystal classes contain permanent dipole moments, which enables the possibility of ferroelectricity [2] and pyroelectricity. [3]. While the chirality of [R-aqnH_2]$^{2+}$ and [S-aqnH_2]$^{2+}$ imparts noncentrosymmetry to **1a** and **1b**, it is the nature of the hydrogen-bonding networks between these cations and [$V_2Te_2O_{10}$]$_n^{2n-}$ layers that is responsible for crystallization in the polar space group $P2_1$ (No. 4, crystal class 2).

The [R-aqnH_2]$^{2+}$ and [S-aqnH_2]$^{2+}$ cations are aligned perpendicular to the [$V_2Te_2O_{10}$]$_n^{2n-}$ layers in order to maximize the strength of the hydrogen-bonding networks (see Fig. 3). The sterically hindered tertiary amines on the [aqnH_2]$^{2+}$ cations hydrogen bond to the [$V_2Te_2O_{10}$]$_n^{2n-}$ layers on the face opposite the bulky stereoactive lone pairs. In contrast, the less crowded primary amines hydrogen bond to the [$V_2Te_2O_{10}$]$_n^{2n-}$ layers on the face containing the stereoactive lone pairs. This has two effects. First, all [R-aqnH_2]$^{2+}$ or [S-aqnH_2]$^{2+}$ cations in a given *inter*-layer spacing have the same orientation because the orientations of the stereoactive lone pairs in a given layer are aligned. Second, neighboring layers are also aligned because each [aqnH_2]$^{2+}$ cation interacts with two different faces of adjacent [$V_2Te_2O_{10}$]$_n^{2n-}$ layers. The result of this is the formation of a polar structure.

While the calculation of dipole moments on individual polar units in a compound is illustrative, the degree to which neighboring dipoles cancel with one another shares equal importance. As stated above, the alignment or misalignment of neighboring dipoles directly affects the physical properties of a given compound. The major contributors to the *net* dipole moments in **1a** and **1b** are the [$V_2Te_2O_{10}$]$_n^{2n-}$ layers. See Fig. 3 and Table 4.

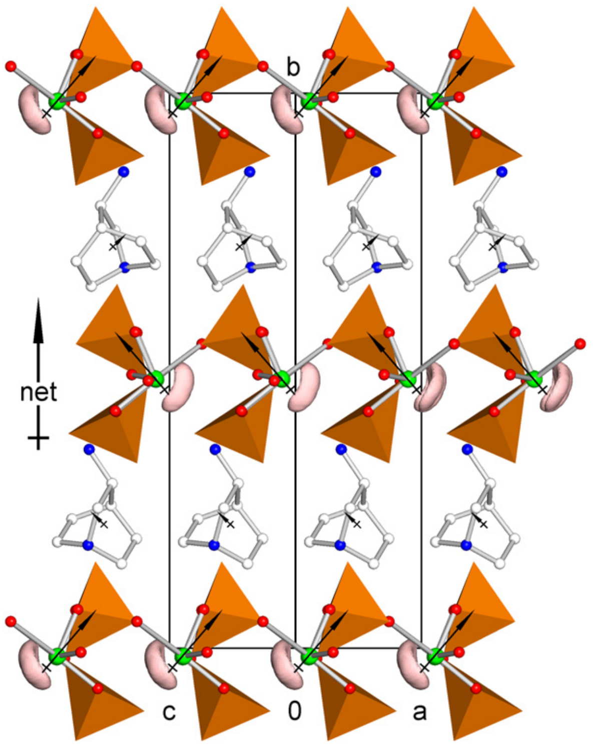

Fig. 3. Three-dimensional packing in **1a**. ELF isosurfaces are shown with a boundary condition of 0.78. Hydrogen atoms have been removed for clarity. The black arrows indicate the approximate directions and magnitudes of the dipole moments for the $[(VO_2)_2O(TeO_4)_2]$ monomers and $[aqnH_2]^{2+}$ cations. The large black arrow represents the net dipole moment in **1a**.

The presence of 2_1 screw axes in each enantiomer, perpendicular to the plane of layer propagation, results in a 180° rotation of the $[V_2Te_2O_{10}]_n^{2n-}$ layers, the organic cations and their respective dipole moments every $b/2$. This forces cancellation of any dipole moment contributions in directions other than along the b-axis. In fact, the direction of the *net* dipole is fixed along the crystallographic b-axis by the symmetry of the structure. A significant component of the dipole moments on the $[V_2Te_2O_{10}]_n^{2n-}$ layers in **1a** and **1b** lie along the b-axis, resulting in *net* moments of 17.37 and 16.62D, respectively.

The observation that little cancellation occurs between the largest component dipole moments in **1a** and **1b** is a result of the $[R\text{-aqnH}_2]^{2+}$ and $[S\text{-aqnH}_2]^{2+}$ cations. While their dipole moments are both significantly smaller than the inorganic layers, these cations are responsible for alignment of the $[V_2Te_2O_{10}]_n^{2n-}$ layers along the b-axis, as described above. The net moments in the anionic $[V_2Te_2O_{10}]_n^{2n-}$ layers and either $[R\text{-aqnH}_2]^{2+}$ or $[S\text{-aqnH}_2]^{2+}$ cations form attractive dipole–dipole electrostatic interactions. In addition, an extensive hydrogen-bonding network is formed between the organic cations and the $[V_2Te_2O_{10}]_n^{2n-}$ oxides, all of which are negatively charged and are possible hydrogen bond acceptors.

Plots of the SHG intensities versus particle size for **1a** and **1b** are shown in Fig. 4. These enantiomers exhibit SHG intensities that are $\sim 50 \times \alpha\text{-SiO}_2$ (the reference used in this study), and both display type 1 phase-matching capabilities.

The use of racemic aqn in reactions that are identical to those that resulted in the formation of **1a** and **1b** could result in several possible outcomes. First, resolution of the $[R\text{-aqnH}_2]^{2+}$ and $[S\text{-aqnH}_2]^{2+}$ cations could result in a mixture of **1a** and **1b**, in an analogous fashion to Pasteur's separation of sodium ammonium tartrate [69,70]. Second, the formation of a distinct phase, in which the $[R\text{-aqnH}_2]^{2+}$ and $[S\text{-aqnH}_2]^{2+}$ cations are related to one another through inversion symmetry, could occur. This behavior has been observed in templated polyoxomolybdates [65] and gallium phosphates [64]. Third, the $[R\text{-aqnH}_2]^{2+}$ and $[S\text{-aqnH}_2]^{2+}$ cations could form domains within each crystal, resulting in an inversion twin, as observed in some templated molybdenum sulfates [66,67].

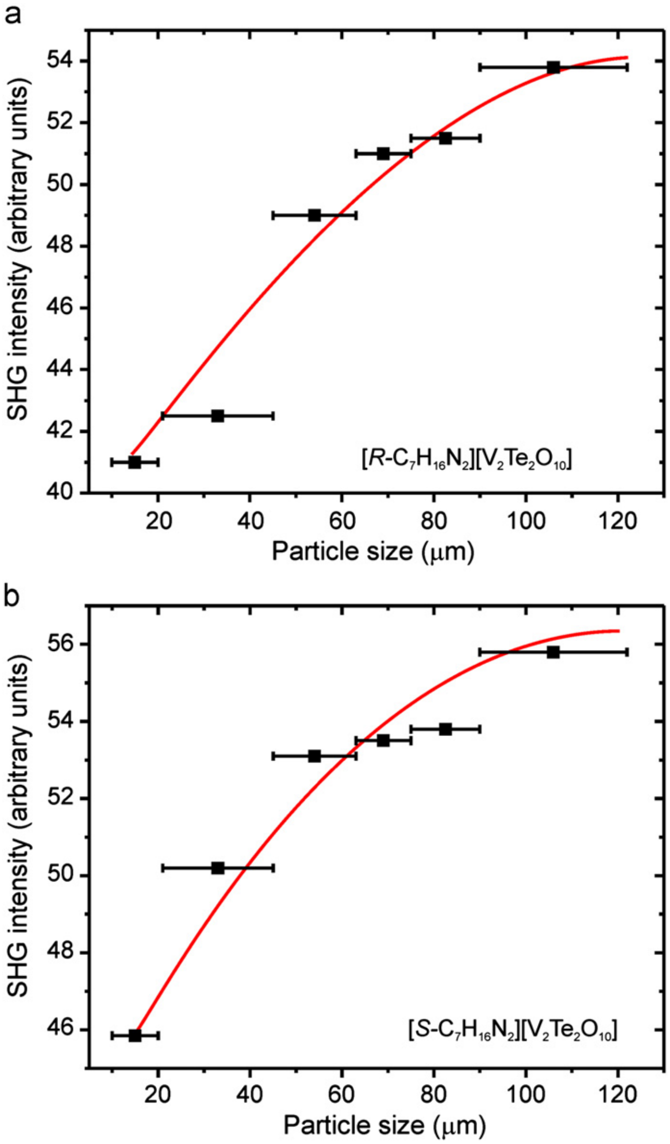

Fig. 4. SHG intensity versus particle size data for (a) **1a** and (b) **1b**. The curves drawn are to guide the eye and are not fits of the data.

The use of racemic aqn in this study resulted in the formation of low quality crystals, despite repeated attempts to improve sample quality. The powder X-ray diffraction patterns of the racemate are essentially identical to those of **1a** and **1b**. In addition, the racemate was found to display type 1 phase-matching capabilities and an SHG activity essentially equivalent to **1a** and **1b**. This suggests either the formation of inversion twins or the partial resolution of the $[R\text{-aqnH}_2]^{2+}$ and $[S\text{-aqnH}_2]^{2+}$ cations and the formation of a mixture of **1a** and **1b**. The formation of a distinct, centrosymmetric phase in which the $[R\text{-aqnH}_2]^{2+}$ and $[S\text{-aqnH}_2]^{2+}$ cations are related to one another through inversion symmetry did not occur because such a phase would not be SHG active. Unfortunately, the low crystal quality precludes additional structural characterization. A plot of the SHG intensity versus particle size for the racemate is available in the Supplementary Data.

5. Conclusion

Hydrogen-bonding between either $[R\text{-aqnH}_2]^{2+}$ or $[S\text{-aqnH}_2]^{2+}$ cations and $[V_2Te_2O_{10}]_n^{2n-}$ layers results in the formation of polar, noncentrosymmetric structures. The application of iterative Hirshfeld charge partitioning to these organic inorganic structures resulted in better atomic partial charges, from which both local and *net* dipole moments were calculated.

Acknowledgments

The authors acknowledge support from the NSF (Award no. CHE-0911121) and grants to Haverford College from the HHMI Undergraduate Science Education Program. A.J.N. acknowledges the Henry Dreyfus Teacher-Scholar Awards Program. J.Y. and P.S.H. acknowledge the Robert A. Welch Foundation (Grant E-1457), the ACS PRF 47345-AC10) and the NSF (DMR-0652150) for support. M.Z. acknowledges support for the purchase of a diffractometer from the NSF grant 0087210, the Ohio Board of Regents grant CAP-491 and from Youngstown State University. This research used resources of the National Energy Research Scientific Computing Center, which is supported by the Office of Science of the U.S. Department of Energy under Contract No. DE-AC02-05CH11231.

Supplementary Data

Crystallographic data (excluding structure factors) for the structures reported in this paper have been deposited with the Cambridge Crystallographic Data Center as supplementary publication no. CCDC 799313 and 799314. Tables of bond valence sums, calculated atomic Hirshfeld and Hirshfeld-I charges and thermogravimetric traces for **1a** and **1b**, figures of $[R\text{-aqnH}_2]^{2+}$ and $[S\text{-aqnH}_2]^{2+}$ dipole moments and a SHG intensity versus particle size plot for $[C_7H_{16}N_2][V_2Te_2O_{10}]$ are available in the Supplementary Data.

Appendix A. Supporting information

Supplementary data associated with this article can be found in the online version at doi:10.1016/j.jssc.2011.04.016.

References

[1] P.S. Halasyamani, K.R. Poeppelmeier, Chem. Mater. 10 (1998) 2753–2769.
[2] O. Auciello, J.F. Scott, R. Ramesh, Phys. Today 51 (1998) 22–27.
[3] S.B. Lang, Phys. Today 58 (2005) 31–36.
[4] J. Yeon, S.-H. Kim, P.S. Halasyamani, Inorg. Chem. 49 (2010) 6986–6993.
[5] S.-H. Kim, J. Yeon, P.S. Halasyamani, Chem. Mater. 21 (2009) 5335–5342.
[6] H.-Y. Chang, S.-H. Kim, K.M. Ok, P.S. Halasyamani, J. Am. Chem. Soc. 131 (2009) 6865–6873.
[7] T. Sivakumar, H.Y. Chang, J. Baek, P.S. Halasyamani, Chem. Mater. 19 (2007) 4710–4715.
[8] T. Sambrook, C.F. Smura, S.J. Clarke, K.M. Ok, P.S. Halasyamani, Inorg. Chem. 46 (2007) 2571–2574.
[9] J.-H. Kim, J. Baek, P.S. Halasyamani, Chem. Mater. 19 (2007) 5637–5641.
[10] H.-L. Jiang, S.-P. Huang, Y. Fan, J.-G. Mao, W.-D. Cheng, Chem. Eur. J. 14 (2008) 1972–1981.
[11] R.G. Pearson, J. Am. Chem. Soc. 91 (1969) 4947–4955.
[12] R.A. Wheeler, M.H. Whangbo, T. Hughbanks, R. Hoffmann, J.K. Burdett, T.A. Albright, J. Am. Chem. Soc. 108 (1986) 2222–2236.
[13] M. Kunz, I.D. Brown, J. Solid State Chem. 115 (1995) 395–406.
[14] P.-X. Li, S.-Y. Zhang, J.-G. Mao, Dalton Trans. 39 (2010) 11560–11567.
[15] P.-X. Li, F. Kong, C.-L. Hu, N. Zhao, J.-G. Mao, Inorg. Chem. 49 (2010) 5943–5952.
[16] S.-Y. Zhang, C.-L. Hu, C.-F. Sun, J.-G. Mao, Inorg. Chem. 49 (2010) 11627–11636.
[17] J.-Y. Xie, J.-G. Mao, Inorg. Chem. Commun. 8 (2005) 375–378.
[18] H.-L. Jiang, F. Kong, Y. Fan, J.-G. Mao, Inorg. Chem. 47 (2008) 7430–7437.
[19] H.Y. Chang, S.-H. Kim, K.M. Ok, P.S. Halasyamani, Chem. Mater. 21 (2009) 1654–1662.
[20] T. Sivakumar, K.M. Ok, P.S. Halasyamani, Inorg. Chem. 45 (2006) 3602–3605.
[21] P.S. Halasyamani, D. O'Hare, Inorg. Chem. 36 (1997) 6409–6412.
[22] C.R. Jeggo, G.D. Boyd, J. Appl. Phys. 41 (1970) 2741–2743.
[23] B.F. Levine, Phys. Rev. B 7 (1973) 2600–2626.
[24] C.T. Chen, G.Z. Liu, Annu. Rev. Mater. Sci. 16 (1986) 203–243.
[25] P.A. Maggard, T.S. Nault, C.L. Stern, K.R. Poeppelmeier, J. Solid State Chem. 175 (2003) 27–33.
[26] H.K. Izumi, J.E. Kirsch, C.L. Stern, K.R. Poeppelmeier, Inorg. Chem. 44 (2005) 884–895.
[27] M.R. Marvel, J. Lesage, J. Baek, P.S. Halasyamani, C.L. Stern, K.R. Poeppelmeier, J. Am. Chem. Soc. 129 (2007) 13963–13969.
[28] R. Evans Owen, W. Lin, Acc. Chem. Res. 35 (2002) 511–522.
[29] B. Moulton, M.J. Zaworotko, Chem. Rev. 101 (2001) 1629–1658.
[30] J.S. Knyrim, P. Becker, D. Johrendt, H. Huppertz, Angew. Chem. Int. Ed. 45 (2006) 8239–8241.
[31] S. Pan, Y. Wu, P. Fu, G. Zhang, Z. Li, C. Du, C. Chen, Chem. Mater. 15 (2003) 2218–2221.
[32] C. Chen, Y. Wang, B. Wu, K. Wu, W. Zeng, L. Yu, Nature 374 (1995) 290.
[33] Y. Porter, K.M. Ok, N.S.P. Bhuvanesh, P.S. Halasyamani, Chem. Mater. 13 (2001) 1910–1915.
[34] N. Ye, Q. Chen, B. Wu, C. Chen, J. Appl. Phys. 84 (1998) 555–558.
[35] O.K. Andersen, Phys. Rev. B 12 (1975) 3060–3083.
[36] O.K. Andersen, O. Jepsen, Phys. Rev. Lett. 53 (1984) 2571–2574.
[37] *Apex2 v2009.7-0.*, Bruker AXS Inc., Madison (WI), USA, 2009.
[38] A. Altomare, G. Cascarano, C. Giacovazzo, A. Guagliardi, J. Appl. Crystallogr. 26 (1993) 343–350.
[39] P.W. Betteridge, J.R. Carruthers, R.I. Cooper, K. Prout, D.J. Watkin, J. Appl. Crystallogr. 36 (2003) 1487.
[40] E. Dowty, *ATOMS v. 6.0*, Shape Software, TN, USA, 2002.
[41] S.K. Kurtz, T.T. Perry, J. Appl. Phys. 39 (1968) 3798–3813.
[42] M. Kohout, A. Savin, J. Comput. Chem. 18 (1997) 1431–1439.
[43] K.B. Chang, D.J. Hubbard, M. Zeller, J. Schrier, A.J. Norquist, Inorg. Chem. 49 (2010) 5167–5172.
[44] X. Gonze, J.M. Beuken, R. Caracas, F. Detraux, M. Fuchs, G.M. Rignanese, L. Sindic, M. Verstraete, G. Zerah, F. Jollet, M. Torrent, A. Roy, M. Mikami, P. Ghosez, J.Y. Raty, D.C. Allan, Comput. Mater. Sci. 25 (2002) 478–492.
[45] X. Gonze, G.-M. Rignanese, M. Verstraete, J.-M. Beuken, Y. Pouillon, R. Caracas, F. Jollet, M. Torrent, G. Zerah, M. Mikami, P. Ghosez, M. Veithen, J.-Y. Raty, V. Olevano, F. Bruneval, L. Reining, R. Godby, G. Onida, D.R. Hamann, D.C. Allan, Z. Kristallogr. 220 (2005) 558–562.
[46] F.L. Hirshfeld, Theor. Chim. Acta 44 (1977) 129–138.
[47] P. Bultinck, C. Van Alsenoy, P.W. Ayers, R. Carbo-Dorca, J. Chem. Phys. 126 (2007) 144111.
[48] P. Bultinck, P.W. Ayers, S. Fias, K. Tiels, C. Van Alsenoy, Chem. Phys. Lett. 444 (2007) 205–208.
[49] C. Froese Fischer, G. Gaigalas, Comput. Phys. Commun. 98 (1996) 255–264.
[50] K. Jung, H. Kim, H. Yun, J. Do, Z. Anorg. Allg. Chem. 632 (2006) 1582–1585.
[51] M.-L. Feng, J.-G. Mao, J. Solid State Chem. 178 (2005) 2256–2261.
[52] X. Huang, Z. Liu, C. Huang, L. Shen, X. Yan, Acta Crystallogr. Sect. C C65 (2009) m385–m387.
[53] G.-X. Han, Y.-J. Song, Z.-B. Han, J. Solid State Chem. 182 (2009) 2202–2207.
[54] I.D. Brown, D. Altermatt, Acta Crystallogr. Sect. B 41 (1985) 244–247.
[55] N.E. Brese, M. O'Keeffe, Acta Crystallogr. Sect. B 47 (1991) 192–197.
[56] J.K. Burdett, T.A. McCormick, J. Phys. Chem. A 102 (1998) 6366–6372.
[57] B. Silvi, A. Savin, Nature 371 (1994) 683–686.
[58] B. Courcot, A.J. Bridgeman, Int. J. Quant. Chem. 110 (2010) 2155–2161.
[59] S. Van Damme, P. Bultinck, S. Fias, J. Chem. Theor. Comput. 5 (2009) 334–340.
[60] O. Leenaerts, B. Partoens, F.M. Peeters, Appl. Phys. Lett. 92 (2008) 243125/243121-243125/243123.
[61] K.M. Ok, P.S. Halasyamani, Inorg. Chem. 43 (2004) 4248–4253.
[62] C.J. Kepert, T.J. Prior, M.J. Rosseinsky, J. Am. Chem. Soc. 122 (2000) 5158–5168.
[63] M. Inoue, T. Yamase, Bull. Chem. Soc. Jpn. 68 (1995) 3055–3063.
[64] S.J. Choyke, S.M. Blau, A.A. Larner, A. Narducci Sarjeant, J. Yeon, P.S. Halasyamani, A.J. Norquist, Inorg. Chem. 48 (2009) 11277–11282.
[65] T.R. Veltman, A.K. Stover, A. Narducci Sarjeant, K.M. Ok, P.S. Halasyamani, A.J. Norquist, Inorg. Chem. 45 (2006) 5529–5537.
[66] E.A. Muller, R.J. Cannon, A. Narducci Sarjeant, K.M. Ok, P.S. Halasyamani, A.J. Norquist, Cryst. Growth Des. 5 (2005) 1913–1917.
[67] J.R. Gutnick, E.A. Muller, A. Narducci Sarjeant, A.J. Norquist, Inorg. Chem. 43 (2004) 6528–6530.
[68] D.J. Hubbard, A.R. Johnston, H. Sanchez Casalongue, A. Narducci Sarjeant, A.J. Norquist, Inorg. Chem. 47 (2008) 8518–8525.
[69] L. Pasteur, Ann. Chim. Phys. 24 (1848) 442–459.
[70] L. Pasteur, Ann. Chim. Phys. 28 (1850) 56–99.